Check for updates

ADVANCED FUNCTIONAL MATERIALS
www.afm-journal.de

Unveiling the Nanoarchitectonics of Interfacial Electronic Coupling in Atomically Thin 2D WO_3/WSe_2 Heterostructure for Sodium-Ion Storage in Aqueous System

Pragati A. Shinde, Vikram Mahamiya, Moein Safarkhani, Nilesh R. Chodankar, Masaki Ishii, Renzhi Ma, Amal Al Ghaferi, Lok Kumar Shrestha,* and Katsuhiko Ariga**

Aqueous sodium (Na^+) ion storage systems face challenges due to sluggish adsorption and diffusion of Na^+ ions with larger size, hindering their potential for stationary applications. This issue is addressed by evolving the interfacial electronic coupling in atomically thin 2D WO_3/WSe_2 heterostructure for efficient Na^+ ion storage. Density functional theory (DFT) analysis elucidates the superior charge storage capability for the WO_3/WSe_2 heterostructure facilitated by the charge transfer from the WO_3 – WSe_2 (002). The charge transfer from the W-5d and O-2p orbitals of WO_3 to the valence W-5d and Se-4p orbitals of the WSe_2 (002) surface boosts the electronic conductivity. As a result, the WO_3/WSe_2 electrode demonstrates exceptional Na^+ ion storage, with a specific capacitance of 378.1 F g^{-1} at 1 A g^{-1}, excellent rate capability, and long-lasting cycling durability. The full cell comprising WO_3/WSe_2 as the negative and MnSe/$MnSe_2$ as the positive electrode achieved a peak energy density of 82.1 Wh kg^{-1} at a power density of 1873.5 W kg^{-1}, along with high rate capability and long-cycle durability. Insights gained from this study pave the technique for the rational design and optimization of the interfacial electronic features in 2D heterostructures for next-generation energy storage devices with enhanced performance and stability.

1. Introduction

Electrical energy storage (EES) systems are a promising and significant class of energy storage technologies. They offer advantages in safety, cost-effectiveness, scalability, and environmental sustainability.[1] EES systems can store and supply intermittent power, making them useful in electric vehicles (EVs), large-scale energy storage for power generation, and consumer electronics. Numerous EES systems have been developed, unveiling different charge storage mechanisms and application areas. Among them, electrochemical capacitors (ECs) dominate in meeting high-power demands, while rechargeable lithium-ion batteries (LIBs) excel in storing high-energy.[2] Remarkably, next-generation aqueous metal-ion energy storage systems utilizing metals such as sodium, zinc, potassium, magnesium, and aluminum are expected to become the primary choice for

---

P. A. Shinde, M. Ishii, R. Ma, L. K. Shrestha, K. Ariga
Research Center for Materials Nanoarchitectonics (MANA)
National Institute for Materials Science (NIMS)
1-1 Namiki, Tsukuba 305-0044, Japan
E-mail: shinde.pragatiankush@nims.go.jp;
shrestha.lokkumar@nims.go.jp; ariga.katsuhiko@nims.go.jp

V. Mahamiya
The Abdus Salam International Centre for Theoretical Physics (ICTP)
Trieste I-34151, Italy

M. Safarkhani
NanoBio High-Tech Materials Research Center
Department of Biological Sciences and Bioengineering
Inha University
Incheon 22212, Republic of Korea

The ORCID identification number(s) for the author(s) of this article can be found under https://doi.org/10.1002/adfm.202406333

DOI: 10.1002/adfm.202406333

N. R. Chodankar
Mechanical Engineering Department
Khalifa University of Science and Technology
Abu Dhabi 127788, United Arab Emirates

A. A. Ghaferi
Rabdan Academy
Abu Dhabi 114646, United Arab Emirates

L. K. Shrestha
Department of Materials Science
Institute of Pure and Applied Sciences
University of Tsukuba
1-1-1, Tsukuba 305-8573, Japan

K. Ariga
Graduate School of Frontier Sciences
The University of Tokyo
5-1-5 Kashiwanoha, Kashiwa, Chiba 277-8561, Japan

a sustainable yet safe future.[3] Considering this advantage, most recently, aqueous sodium-ion capacitors (ASIC) are particularly promising owing to the richness of sodium resources and compatibility with existing industrial systems.[4] ASIC consists of a battery/pseudocapacitive anode and a capacitive cathode. However, ASIC faces challenges because of the sluggish reaction kinetics among intercalation-type and electric double-layer capacitor (EDLC)-type electrodes. This challenge is more pronounced for ASIC because of the large radius of Na^+ ions (1.02 A), hindering their redox kinetics for high-rate performance. Developing pseudocapacitive cathodes and anodes with wide interlayer spacings for Na^+ ion storage could significantly improve ASIC energy density and rate performance. The pseudocapacitive mateials are fascinating and the research related to the pseudocapacitive materials hasn't received as much attention as it deserves. With the right materials, we could unlock new levels of performance and efficiency in these integrated circuits.

Pseudocapacitive materials are redox-active, just like battery materials. The only difference is that pseudocapacitive materials can store the charge quickly, like conventional EDLCs, but with higher energy storage capacity.[5] However, when it comes to Na^+ ion storage, there are a few challenges associated with pseudocapacitive materials. Fabricating pseudocapacitive materials with desired morphologies, compositions, and structures can be challenging. Moreover, the prepared pseudocapacitive materials ensure that good electrolyte wetting, facial ion transport, and stable interfacial interactions in Na^+ ions based electrolytes are critical for achieving optimal storage performance. Among various pseudocapacitive materials, the transition metal dichalcogenides (TMDs) with layered structures offer 2D networks for Na^+ ion intercalation/deintercalation and storage.[6] The reversible redox reactions of Na^+ ions into layered materials were first stated in the early 1980s.[7] Layered TMDs, specifically metal selenides (MSe_x), show great promise in electrochemistry owing to their earth abundance, cost-effectiveness, high stability, and high theoretical capacity.[8] Relative to metal oxides, M—X (X = S, Se) bonds are weaker and more conducive to charge transfer reactions. In MSe_x, a metal atom is bonded with two selenide layers to form a sandwich structure (Se-M-Se), and neighboring Se-M-Se layers are held together by weak van der Waals forces.[9] The considerable interlayer distance and weak interaction enable alkali ions to migrate quickly with low diffusion barriers, allowing for easy intercalation reactions.[10] Besides its inherent structural qualities that boost diffusion rates, the outstanding capability of the electrode to store Na^+ ions also benefits from its favorable conductivity.[11] Compared with the metal sulfides, the MSe_x with Se atoms has a larger atomic radius and more robust metallic properties than sulfur atoms, leading to metal selenides with increased interlayer spacing and improved electronic conductivity.[12]

A practical approach to improve Na^+ ions storage performance in TMDs is to enlarge the interlayer distance to enable Na^+ ion diffusion.[13] Among MSe_x, WSe_2 stands out as one of the extensively researched materials because of its simple synthesis and large interlayer distance (0.62 nm).[14] Despite its promising electronic properties, the intrinsic conductivity may not be sufficient for high-performance ASIC, potentially leading to sluggish charge transfer kinetics and limited electrochemical performance. Different approaches have been proposed to address this issue, such as nanostructure tuning, doping, surface modification, etc.[15] Internal interface modification techniques are one of the most effective ways to enlarge lattice spacings to improve the electron/ion transport performance.[16] With this outline, heterostructures formed by combining materials with different band gaps (e.g., WO_3 – 2.6 eV, WSe_2: 1.6 – eV), show promising potential in Na^+ ions storage performance. These structures enable the formation of tailored heterointerfaces, enhancing the diffusion of large intercalated ions (e.g., Na^+, Mg^{2+}, Zn^{2+}), reducing charge transfer resistance, and enhancing structural flexibility during intercalation/extraction processes.[17] Notably, the spontaneous generation of an inherent electric field and pseudocapacitance rising from quick redox reactions offer fast charge–discharge rates. For instance, Jung et al.[18] designed self-assembled 1D WO_3/2D WS_2 core-shell interfaces, demonstrating superior cycling stability in hybrid supercapacitors due to the rapid Na^+ ion transfer. Xavier et al.[19] developed a reduced graphene oxide/WO_3/WS_2 nanocomposite, enhancing ion transport at the heterojunction interface and achieved a specific capacitance of 750 F g^{-1} at 10 mV s^{-1} and excellent rate performance. Heterostructures such as $MoO_2/MoSe_2$,[20] MoO_3/MoS_2,[21] MoS_2/WS_2,[22] $Ti_3C_2T_x/WSe_2$,[23] and so forth have been developed recently, exhibiting improved charge storage performance. Although the benefits of intrinsic interface regulation in the heterostructures mentioned above are clear, the combined effect of interface and heterostructure engineering on aqueous Na-based systems remains poorly understood. Further studies are needed to understand how tuning interfaces and charge storage in layered materials can increase the energy density and rate performance of ASIC.

We have created atomically thin 2D nanosheets of WO_3/WSe_2 heterostructures efficiently using a scalable yet simple hydrothermal method which was followed by chemical vapor deposition (CVD) directly on the carbon fiber (CF) substrate for efficient storage of Na^+ ions. The integration of WO_3/WSe_2 heterostructures overcomes the challenge of sluggish adsorption and diffusion of large-sized Na^+ ions. Density functional theory (DFT) calculations corroborate these findings, elucidating the superior electrochemical performance of WO_3/WSe_2 heterostructures, primarily attributed to charge transfer from the O-atoms of WO_3 to the W-5d and Se-4p-orbitals of the WSe_2 (002) surface. Benefiting from the large interlayer spacings and improved electronic conductivity, the WO_3/WSe_2 heterostructures deliver a specific capacitance of 378.1 F g^{-1} at 1 A g^{-1}, excellent rate performance, and long-cycle durability. Further, the developed ASIC full cell achieved an energy density of 82.1 Wh kg^{-1} at a power density of 1873.5 W kg^{-1} and maintained 53.3 Wh kg^{-1} at 18735.4 W kg^{-1}, respectively.

2. Results and Discussion

The synthesis protocol for growing 2D WO_3/WSe_2 heterostructures directly on CF substrate is illustrated in **Figure 1a**. To systematically study the consequence of selenization temperature on the growth of WSe_2 nanoflakes, crystallographic structure and Na^+ ion storage performance, a series of WO_3/WSe_2 samples were prepared under identical conditions with temperature variations. Initially, WO_3 is grown on a CF substrate using a hydrothermal method, following procedures detailed in our

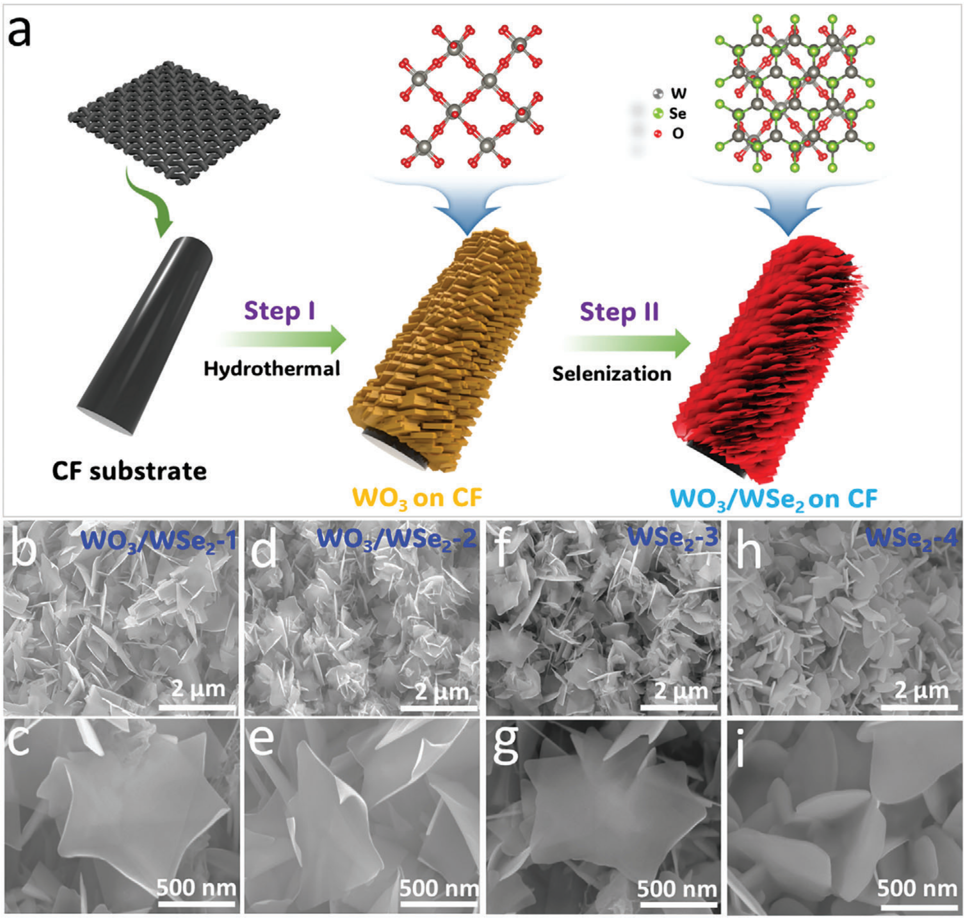

Figure 1. a) Two-step synthesis protocol of the WO_3/WSe_2 heterostructures on CF. low-and high-magnification SEM images of WO_3/WSe_2 heterostructures, b,c) WO_3/WSe_2-1, d,e) WO_3/WSe_2-2, f,g) WSe_2-3 and h,i) WSe_2-4.

previous work.[24] WO_3/CF and Se powder are utilized as precursors for producing WO_3/WSe_2 heterostructures. WO_3/CF is placed in the middle of a tube furnace, which ramped to temperatures ranging from 600 to 900 °C over 10° per minute and held for 2 h to facilitate growth. Simultaneously, Se powder is placed upstream at a lower temperature zone (≈350 °C) for Se evaporation. A flow of 100 sccm N_2 serves as carrier gas throughout the process. The method involves a straightforward inert-atmosphere annealing process under Se vapors, which facilitates partial phase conversion from WO_3 to WSe_2. In this process, Se vapor serves as a reducing agent, promoting the reduction of WO_3 by reacting with oxygen atoms in the WO_3 lattice to form volatile oxides, thereby reducing the oxygen content in the material. The Se^{2-} continuously decomposes WO_3 from the surface to the interior, replacing O^{2-} to form WSe_2. The replacement of O^{2-} is precisely controlled at different temperatures (600, 700, 800, and 900 °C), and induces structural modifications in the material. The resulting samples are denoted as WO_3/WSe_2-1, WO_3/WSe_2-2, WSe_2-3, and WSe_2-4, corresponding to temperatures of 600, 700, 800, and 900 °C, respectively.

Scanning electron microscopy (SEM) was used to analyze the surface morphology of prepared materials, offering insights into the assembly of nanoflakes on CF. SEM images in Figure S1 (Supporting Information) reveal that WO_3 exhibits a stacked sheet-like structure, which is not particularly conducive to Na^+ ions storage. Following the selenization process, WO_3 stacked sheets were transformed into ultrathin nanoflakes, as depicted in Figure 1b-i. Notably, the CF substrate is covered with arrays of WO_3/WSe_2 nanoflakes, with each nanoflake distinctively separated and firmly adhering to the CF. WO_3/WSe_2-1 and WO_3/WSe_2-2 exhibited similar ultrathin nanoflakes morphologies (Figure 1b–e). At high magnification, it became clear that each nanoflake was separated, forming a star-like nanoarchitecture with a lateral size of 500–700 nm and a thickness of less than 5 nm. These nanoflakes effectively alleviate the stacking of Se-W-Se layers, facilitating facile Na^+ ion transport. The ultrathin appearance of these nanoflakes suggests that the presence of WO_3 in the material, i.e., heterophase, dynamically influences nanoflake thickness reduction. Such ultrathin nanoflakes hold potential as electrodes for ASIC, offering a large electroactive surface area, superior stability, and plenty of interspace for Na^+ ion access, enhancing charge storage properties and overall electrochemical performance. Comparatively, the thickness of WSe_2-3 nanoflakes (Figure 1f,g) appeared larger, suggesting that temperature has kinetic influences on nanoflake thickness. Further increase in selenization temperature for WSe_2-4 (Figure 1h,i) resulted in a gradual decrease of nanoflake size and an increase in thickness, indicating that high-temperature selenization

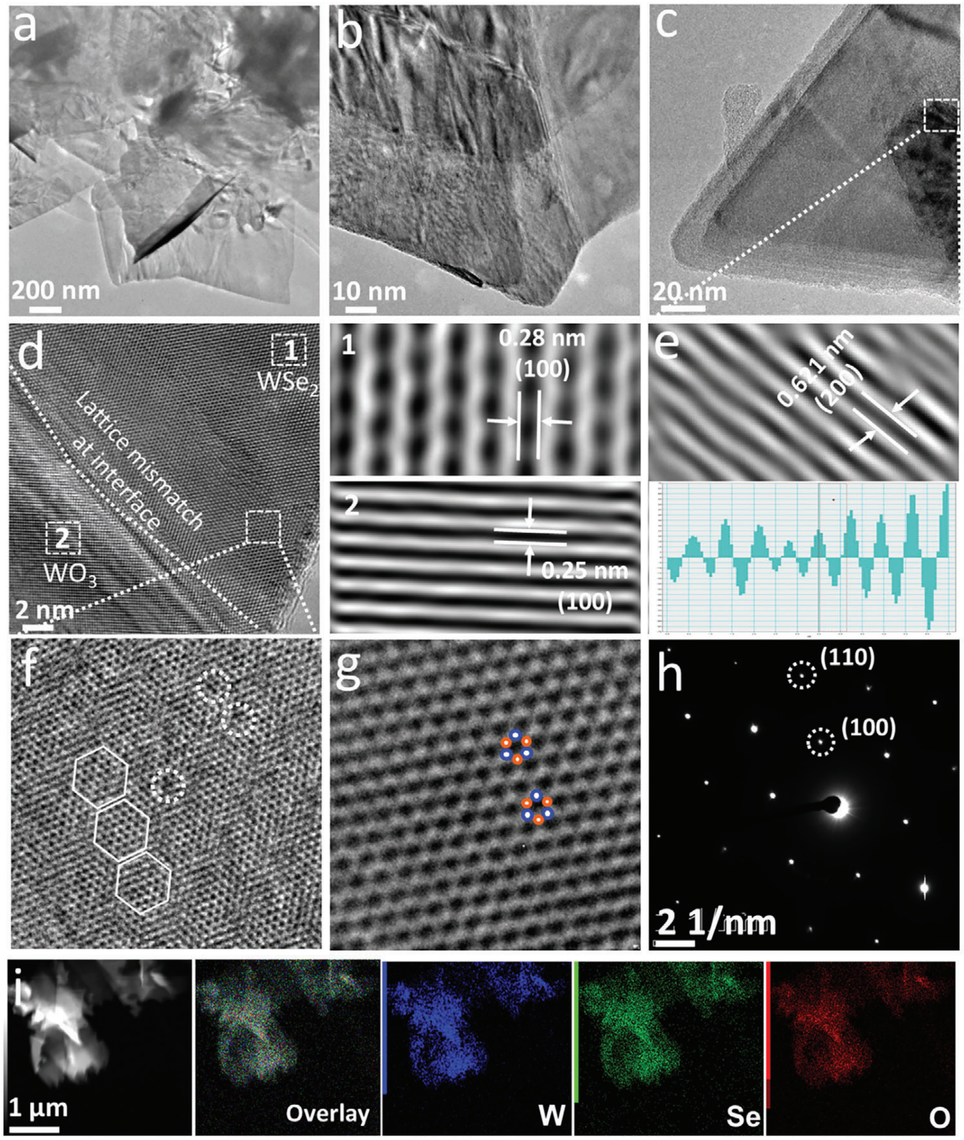

Figure 2. a–c) TEM images of WO_3/WSe_2-2 d–h) HRTEM image with interlayer spacings and corresponding SAED pattern and i) HAADF-STEM image and EDS elemental maps of WO_3/WSe_2-2 heterostructures.

promotes nanoflake miniaturization, ultimately leading to the formation of dense nanosheets. The Energy dispersive X-ray spectroscopy (EDS) spectrum with element atomic% is shown in Figure S2a (Supporting Information). The EDS mapping images for WO_3/WSe_2-2, revealing the uniform dispersal of W, Se, and O elements on CF substrate (Figure S2b–f, Supporting Information).

Furthermore, transmission electron microscopy (TEM) analysis was executed to explore the structure characteristics of WO_3/WSe_2 heterostructures. **Figure** 2a–c presents low-resolution TEM images of one exposed corner of the star-shaped WO_3/WSe_2 heterostructure, clearly revealing the ultrathin nanosheets. Figure 2d provides a high-resolution TEM image of the heterostructure interface at the atomic scale, demonstrating evident lattice mismatch. This mismatch between the WO_3 and WSe_2 interfaces can induce strain within the structure and potentially modify the local electronic structures, impacting the Na^+ ion transfer process. In Figure 2d, the upper side corresponds to WSe_2, while the lower side represents WO_3. The atomic arrangement at the interface indicates the successful synthesis of a well-defined WO_3/WSe_2 heterostructure with a clear interface boundary. Notably, WO_3 nanosheets are inclined to align themselves on the threefold symmetric directions of primary WSe_2, as depicted in the figure. The high-resolution transmission electron microscope (HRTEM) image displays a lattice spacing of 0.25 nm, corresponding to the (100) planes of WO_3 (Figure 2d). The polygonal diffraction patterns exhibit crystal plane spacings of 0.28 nm, aligning with the (100) planes of WSe_2, consistent with reported values for WO_3 and WSe_2.[25] As depicted in the HRTEM result (Figure 2e), an interlayer distance of 0.621 nm was identified for the (200) plane of WSe_2.[26] This lattice spacing is sufficient to accommodate a number of Na^+ ions (1.02 Å). The well-ordered honeycomb structure of WSe_2 is visible in Figure 2f,g. The selected area electron diffraction (SAED) of WO_3/WSe_2-2 demonstrates high crystallinity, with the diffraction rings allocated to (100) and (110) planes of 2H-WSe_2 (Figure 2h).[27] The scanning TEM (STEM) images and corresponding elemental mappings show that W, Se, and O elements are uniformly distributed over the entire nanosheets (Figure 2i). These results indicate the successful formation of WO_3/WSe_2 heterostructures through a simple vapor adsorption/selenization process with WO_3. Notably, numerous defect sites are generated near the WO_3/WSe_2 heterointerface, offering adequate active sites to enable Na^+ ion intercalation and enhance ion/electron diffusion kinetics in ASICs. Additionally, atomic force microscopy (AFM) was conducted to determine the thickness of WO_3/WSe_2-2 nanosheets, as illustrated in Figure S3 (Supporting Information). The AFM images reveal that the WO_3/WSe_2-2 heterostructures are composed of numerous small nanoflakes. Figure S3d (Supporting Information) presents two section profiles marked by black and red lines, indicating that the thickness of the nanoflakes ranges from 8 to 22 nm.

To investigate the impact of selenization treatment at different temperatures on physical properties and chemical compositions, X-ray diffraction (XRD) analysis was performed. The WO_3/WSe_2 nanoflakes were synthesized through the selenization of WO_3 nanoblocks under the N_2 atmosphere, where selenium topochemically substitutes oxygen from WO_3, leading to the formation of WO_3/WSe_2 or WSe_2. The XRD patterns of WO_3/WSe_2-1, WO_3/WSe_2-2, WSe_2-3, and WSe_2-4 are illustrated in **Figure** 3a. After selenization, WO_3/WSe_2-1 and WO_3/WSe_2-2 maintained characteristic diffraction peaks attributed to WO_3 at 2θ values of 22.9°, 23.4°, 24.4°, 28.6°, 33.6°, and 41.5°, corresponding to the (002), (020), (200), (022), (202) and (222) planes of triclinic WO_3 P121/n1 (JCPDS 83-0947).[28] The intensity of these peaks in WO_3/WSe_2-2 was slightly reduced, indicating partial replacement of O sites by Se, profoundly influencing the crystallinity of WO_3. Also, diffraction peaks attributed to WO_3 were decreased in WO_3/WSe_2-2, indicative of lattice distortion caused by heterogeneous interface formation. Notably, peaks observed at 2θ of 13.4°, 31.4°, 37.7°, 41.6°, 47.3°, 55.8°, 57.8°, and 65.5° corresponded to (002), (100), (103), (006), (105), (110), (112), and (108) planes, respectively, for 2H WSe_2 with space group P63/mmc (JCPDS: 38-1388), confirming the formation of WO_3/WSe_2 heterostructures, consistent with HRTEM results.[29] Furthermore, with increasing selenization temperatures for WSe_2-3 and WSe_2-4, characteristic diffraction peaks of WO_3 were replaced by those of WSe_2. XRD refinement analysis conducted using powder X-ray diffraction profile analysis (PDXL) software revealed the concentration of WSe_2 in WO_3/WSe_2-1, WO_3/WSe_2-2, WSe_2-3, and WSe_2-4 as 11.5%, 70.4%, 78.5%, and 92.0%, respectively, indicating increase in WSe_2 content with temperature, ultimately forming pure WSe_2 phase (Figure 3b). Notably, for WSe_2-4, a pure 2H-WSe_2 phase was observed, signifying complete conversion from WO_3 to 2H-WSe_2 through O-to-Se topochemical substitution. Thus, the study elucidates the transformation of WO_3 into WO_3/WSe_2 heterostructures and eventually into pure WSe_2 with increasing selenization temperature, as evidenced by XRD analysis.

The crystal structure and corresponding charge transport features at the interface of the WO_3/WSe_2 heterostructure are presented in Figure 3c. Notably, the layered structures are highly suitable for the intercalation and deintercalation of small-diameter ions. Both WO_3 and 2H-WSe_2 possess layered structures. The redistribution of charges at the heterostructure interface contributes to the feature of interface charge relocation, which forms an electric dipole at the interface.[30] The charge transfer between WO_3 and WSe_2 indicates a strong donor–acceptor contact, thereby enhancing the electrochemical activity and establishing an electric field conducive to charge transport.[31] Van der Waals and electrostatic forces develop a connection between WO_3 and WSe_2 at the interface. Remarkably, the charge transfer across the WO_3 and WSe_2 interface is significantly improved due to the efficient injection of holes from WO_3 into WSe_2. The hybridized W d-orbitals and O p-orbitals donate to the conduction band (CB) minimum from WO_3, while simultaneously, hybridized W d-orbitals and Se p-orbitals contribute to the valence band (VB) maximum from WSe_2. Since the CB of WO_3 is lower than WSe_2, a negative CB offset is developed, ensuring the density of electrons in a higher energy level of WO_3 from the CB level of WSe_2. Consequently, WO_3/WSe_2 heterostructure interface facilitates electron mobility. Thus, because of the exclusive crystal structure and charge transfer mechanism between WO_3 and WSe_2, the WO_3/WSe_2 heterostructure interface exhibits efficient charge transfer, enhanced electrochemical activity, and facilitates electron mobility.

X-ray photoelectron spectroscopy (XPS) analysis was used to investigate the phase formation and element oxidation states, providing insight into the phase configuration. The XPS analysis results of WO_3/WSe_2-1, WO_3/WSe_2-2, WSe_2-3, and WSe_2-4 samples are shown in Figures 3d-f and S3 (Supporting Information). As represented in Figure S4 (Supporting Information), the survey scan spectra validate the occurrence of W, Se, O, and C elements deprived of any impurities. The W 4f core-level spectra of WO_3/WSe_2-1 and WO_3/WSe_2-2 were disentangled into a couple of doublet peaks, equivalent to the binding energies of two W oxidation states. Specifically, the disentangled doublet peaks located at 35.7 and 37.9 eV were allocated to $4f_{7/2}$ and $4f_{5/2}$ orbital electrons of W^{6+} oxidation states for the W-O in WO_3, respectively (Figure 3d).[32] In contrast, the peaks at 32.5 and 34.7 eV are matches to $4f_{7/2}$ and $4f_{5/2}$ orbital electrons of W^{4+} for the W-Se in 2H-WSe_2.[29,33] The peaks associated with WSe_2 exhibit a lower binding energy of 3.2 eV compared to those corresponding to WO_3, validating the movement of electron clouds from the electron-abundant WO_3 to the electron-deficient WSe_2, thereby establishing an inherent electric field at the heterostructure interfaces and enhancing the kinetics of charge transfer.[34] Weak peaks at 37.9 eV observed in WSe_2-3 and WSe_2-4 correspond to surface W-oxide due to oxidation during sample handling. The peaks at 32.5 and 34.7 eV, matched with W^{4+} $4f_{7/2}$ and $4f_{5/2}$ of WSe_2, respectively. In the high-resolution Se 3d spectra, two peaks centered at 54.8 and 55.7 eV are allocated to Se $3d_{5/2}$ and Se $3d_{3/2}$ for W—Se bonding,[35] respectively (Figure 3e). Notably, no peak is observed beyond 58.0 eV, indicating the absence of Se—O bonds and confirming that WO_3 and WSe_2 are interfaced via van der Waals forces.[36] In O 1s spectra (Figure 3f), the central peak situated at 530.7 eV suggests a lattice oxygen (W—O) bond, while a small peak at 531.8 eV can be attributed to defective oxygen (O^{2-}).[37] Overall, the prepared samples predominantly exhibited the 2H-WSe_2 phase, consistent with XRD analysis. This

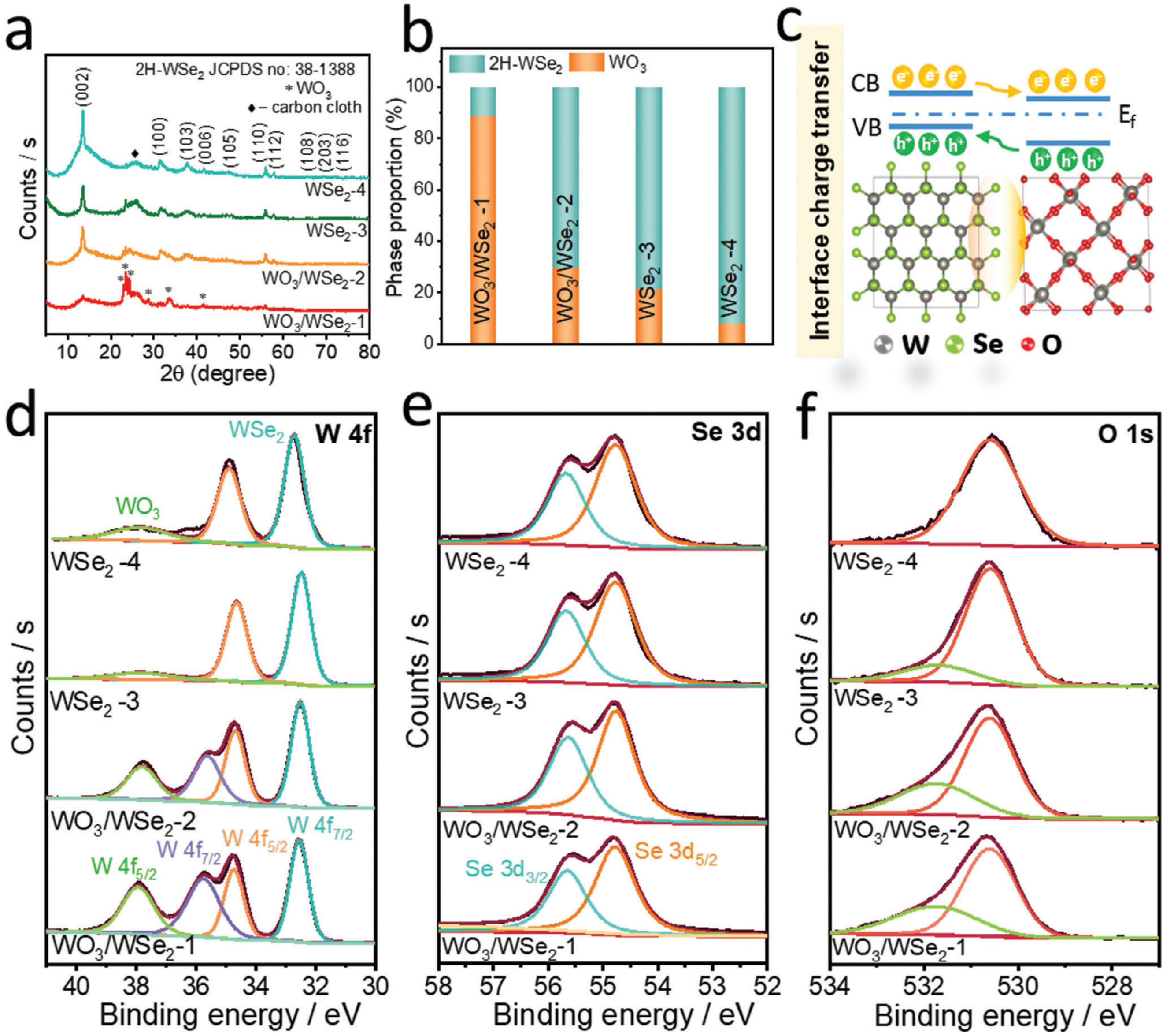

Figure 3. Structural characterizations of WO_3/WSe_2-1, WO_3/WSe_2-2, WSe_2-3, and WSe_2-4. a) XRD patterns and b) WO_3 and WSe_2 phase proportion ration in WO_3/WSe_2-1, WO_3/WSe_2-2, WSe_2-3, and WSe_2-4. c) schematic illustration for charge transfer behavior at WO_3 -WSe_2 heterointerface. Core level XPS spectra of d) W 4f and e) Se 3d f) O 1s in WO_3/WSe_2-1, WO_3/WSe_2-2, WSe_2-3, and WSe_2-4.

observation suggests that the phase conversion from WO_3 to 2H-WSe_2 occurs during high-temperature selenization treatment, as O ions with strong chemisorption properties are replaced by Se.

2.1. Density Functional Theory (DFT) Calculations

We start our calculations by performing the geometry optimization of stable phases of WO_3 and 2H-WSe_2. The WO_3 structure is stabilized in pseudocubic triclinic crystal with lattice parameters a = 7.68 Å, b = 7.69 Å, and c = 7.76 Å, while WSe_2 is hexagonal with lattice parameters a = b = 3.33 Å and c = 13.85 Å. The optimized lattice parameters are matching with the literature.[38] The optimized geometries of WO_3 and WSe_2 are presented in **Figure** 4a,b, respectively. Afterward, we extract the (002) surface slab of WSe_2 since it corresponds to the intense peak of the XRD pattern. We constructed the heterostructure interface of WO_3 –WSe_2 (002) containing two and four atomic layers of WO_3 and WSe_2 (002) surface, corresponding to ≈78% of WSe_2. The optimized geometry of the WO_3-WSe_2 (002) heterostructure is shown in Figure 4c. The differential charge density plot for the WO_3-WSe_2 (002) heterostructure is presented in Figure 4d. This plot corresponds to an isosurface value of 0.160 e Å^{-3}, in which yellow and cyan color regions on the oxygen and tungsten atoms denote the high and low electron densities around these atoms.

We have performed the single point energy calculations using the optimized geometries to investigate the orbitals interactions and charge transfer in the WO_3 –WSe_2 (002) heterostruc-

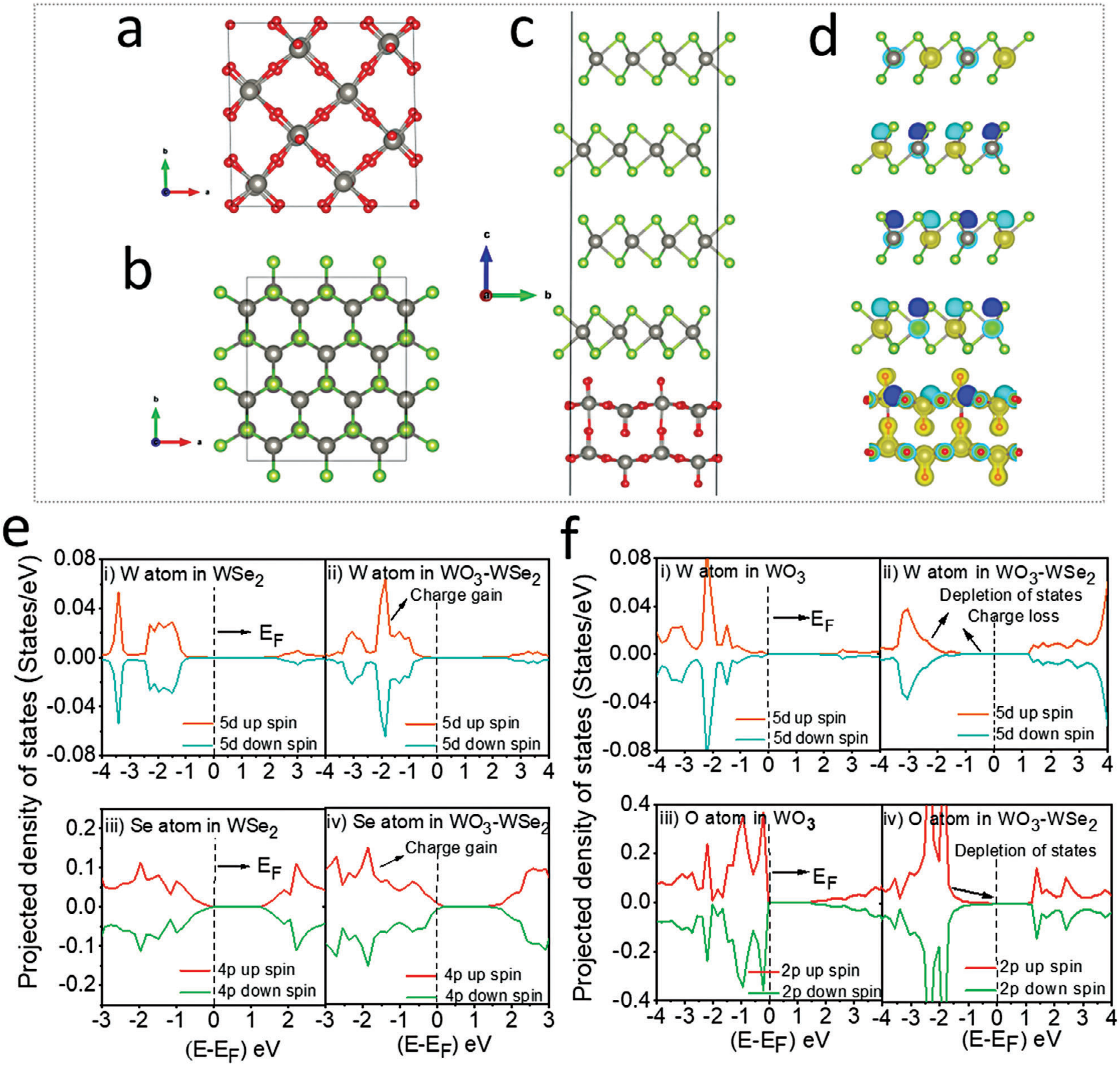

Figure 4. The optimized geometries of a) Top view of WO_3, b) Top view of WSe_2, c) Side view of the interface structure of WO_3 and (002) plane of WSe_2, d) The side view of the differential charge density plot for the complex system for an isosurface value of 0.160 e $Å^{-3}$, where the yellow color denotes the charge accumulation or electron-rich region while cyan color denotes loss of electrons. e) The valence orbitals projected density of states plots for i) 5d orbitals of W in WSe_2 (002), ii) 5d orbitals of W of WSe_2 in $WO_3 - WSe_2$ (002) heterostructure, iii) 4p orbitals of Se in WSe_2 (002) and iv) 4p-orbitals of Se in $WO_3 - WSe_2$ (002) heterostructure. f) The valence orbitals projected density of states plots for i) 5d orbitals of W in WO_3, ii) 5d orbitals of W of WO_3 in $WO_3 - WSe_2$ (002) heterostructure, iii) 2p orbitals of O in WO_3, iv) 2p-orbitals of O in $WO_3 - WSe_2$ (002) heterostructure.

ture. For this purpose, we have plotted the projected density of states (PDOS) of the valence orbitals of W, Se, and O atoms of WSe_2 and WO_3 structures and compared those results with the PDOS of the W, Se, and O atoms in heterostructure WO_3-WSe_2. The PDOS of the 5d and 4p orbitals of W and Se atoms of WSe_2 in WSe_2 (002) slab and WO_3-WSe_2 heterostructures are presented in Figure 4e. It can be seen in Figure 4e ii,iv that the intensity of the W-5d and Se-4p orbital's PDOS in WO_3-WSe_2 heterostructure are significantly enhanced in comparison with the W-5d and Se-4p orbital's PDOS of the WSe_2 (002) slab, particularly in the proximity of Fermi level (−2–0 eV)). Also, the electronic states of these orbitals are shifted toward the Fermi energy in the heterostructure WO_3-WSe_2. This indicates that some charge has been transferred to the valence W-5d and Se-4p orbitals of the WSe_2 slab in the heterostructure WO_3-WSe_2.

To further explore this charge transfer, we plotted the PDOS of the W-5d and O-2p orbitals of WO_3 for WO_3 and WO_3-WSe_2 heterostructure in Figure 4f. We have observed that the W-5d and O-2p orbital's electronic states of WO_3 are depleted in the heterostructure WO_3-WSe_2, near the Fermi energy level −2–0 eV

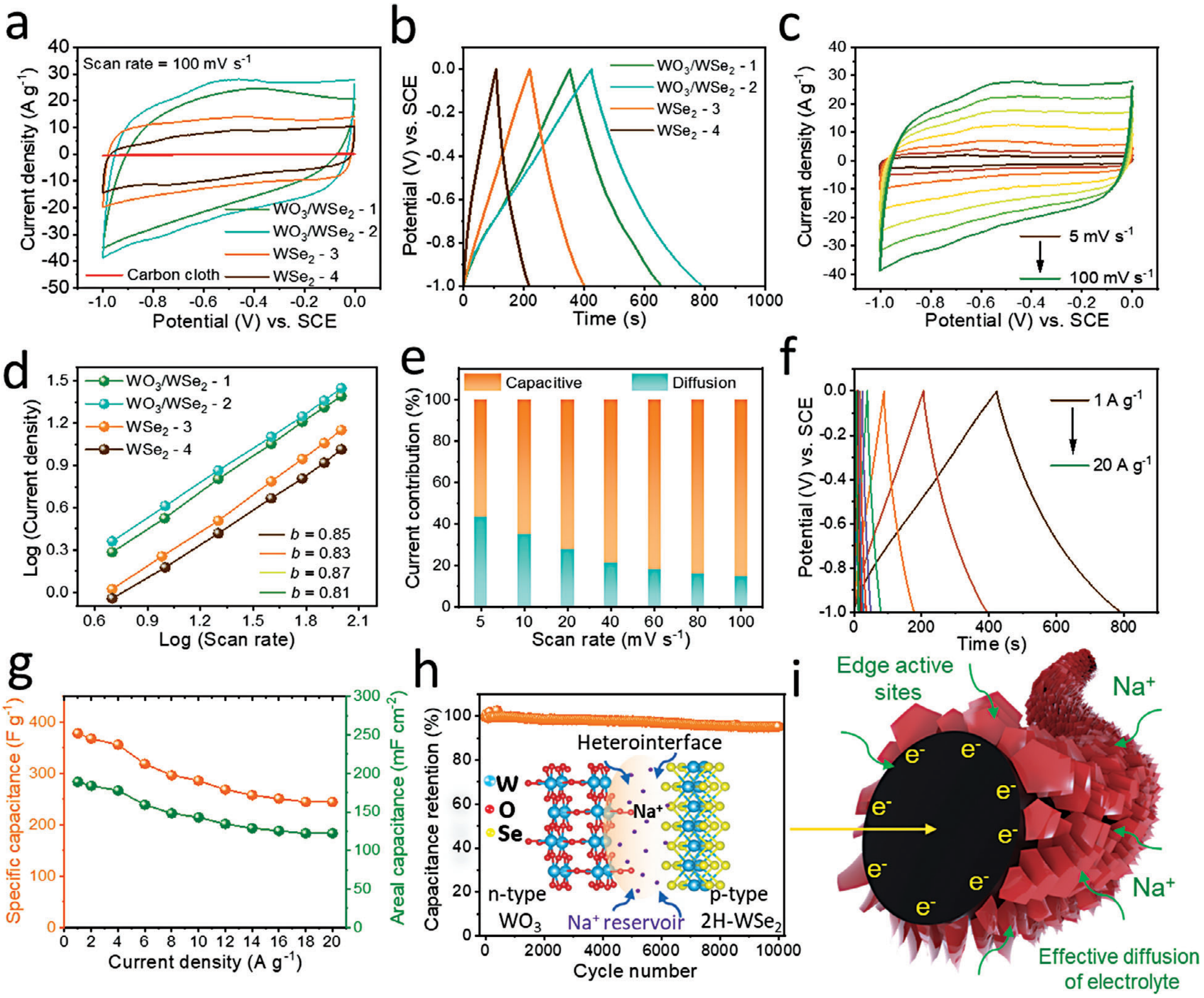

Figure 5. Electrochemical characteristics of WO_3/WSe_2 electrodes. a,b) Comparision of the CV and GCD curves of CF substrate, $WO_3/WSe_2 - 1$, $WO_3/WSe_2 - 2$, $WSe_2 - 3$, and $WSe_2 - 4$ electrodes, c) CV curves at different scan rates. d) calculation of the b-value for $WO_3/WSe_2 - 1$, $WO_3/WSe_2 - 2$, $WSe_2 - 3$, and $WSe_2 - 4$. e) plot of current contribution to the total charge storage at different scan rates for $WO_3/WSe_2 - 2$. f) GCD curves at different current densities for $WO_3/WSe_2 - 2$. g) Specific and areal capacitance of $WO_3/WSe_2 - 2$ obtained from GCD curves. h) Cycling stability at 10 A g^{-1} measured for 10 000 cycles. The inset displays the schematics for the improved electrochemical performance for the $WO_3/WSe_2 - 2$ and i) schematics of Na^+ ion storage in $WO_3/WSe_2 - 2$ heterostructure.

(See Figure 4f ii,iv). This implies that some charge is transferred from the valence W-5d and O-2p orbitals of WO_3 to the W-5d and Se-4p orbitals of WSe_2 (002). This charge transfer is responsible for the superior performance of the WO_3-WSe_2 heterostructure. To quantify this charge transfer, we performed the Bader charge portioning analysis.[39] We report that ≈0.16e electronic charge is transferred from one O-atom of WO_3 to the nearest Se and W atoms of WSe_2.

2.2. Na^+ Ion Storage Performance of WO_3/WSe_2 Heterostructures

Electrochemical measurements were conducted to explore the inherent Na^+ ion storage capabilities of the WO_3/WSe_2 heterostructure. The WO_3/WSe_2 nanoflakes represent optimal candidates for Na^+ ion storage in ASIC due to their distinctive structural features, heterointerfacial boundaries and expanded interplanar spacings. The inherent metallic conductivity of WSe_2 coupled with WO_3 offers significant advantages in facilitating charge transport. At first, Na^+ ion storage characteristics of all materials as electrodes were evaluated in a three-electrode setup using a 2 м $NaClO_4$ electrolyte. **Figure 5a** illustrates the cyclic voltammetry (CV) profiles for CF, $WO_3/WSe_2 - 1$, $WO_3/WSe_2 - 2$, $WSe_2 - 3$, and $WSe_2 - 4$ electrodes across a wide potential range from −1.0 to 0.0 V versus saturated calomel electrode (SCE) at a scan rate of 100 mV s^{-1}. As seen in the comparative CV profiles, the pristine CF substrate had a negligible charge-storing ability, indicating that charge storage occurred primarily in the WO_3/WSe_2-2 materials. The CV profiles of WO_3/WSe_2-2 electrodes exhibit an almost rectangular outline with symmetric loops, suggesting a predominant pseudocapacitive nature. The pseudocapacitive reactions involve electrochemical charge transfer that combines intercalation and deintercalation of Na^+ ions that could be expressed as,[40]

$$WO_3 + xNa^+ + xe^- \leftrightarrow Na_xWO_3 \tag{1}$$

$$Na_xWO_3 + (4-x)\,Na^+ + (4-x)\,e^- \leftrightarrow 2Na_2O_x + W \tag{2}$$

$$WSe_2 + xNa^+ + xe^- \leftrightarrow Na_xWSe_2 \tag{3}$$

$$Na_xWSe_2 + (4-x)\,Na^+ + (4-x)\,e^- \leftrightarrow 2Na_2Se_x + W \tag{4}$$

Notably, the area fenced within the CV curve for WO_3/WSe_2-2 electrode is larger compared to other electrodes, indicating that the WO_3/WSe_2-2 heterostructure have abundant active sites and facilitates more efficient Na^+ ion transfer owing to the heterophase and defects in the WO_3/WSe_2 interface. This suggests enhanced electronic conductivity ascribed to the suitable incorporation of Na^+ ions into and from the layered structure, which is ideal for improving sodium storage performance. This enhancement was further confirmed through galvanostatic charge/discharge (GCD) tests for $WO_3/WSe_2 - 1$, $WO_3/WSe_2 - 2$, $WSe_2 - 3$, and $WSe_2 - 4$ electrodes in a potential window from −1.0 to 0.0 V versus (SCE) at 1 A g^{-1} (Figure 5b). The GCD curves demonstrated a pseudocapacitive behavior characterized by the intercalation/deintercalation of Na^+ ions. The nearly symmetrical GCD curves suggest excellent reversibility in pseudocapacitive reactions. The WO_3/WSe_2-2 electrode exhibited a longer discharge time, ultimately offering high capacitance, consistent with the CV results. The charge transfer between WO_3 and WSe_2 indicates stable donor-acceptor contact, improving the electrochemical activity and creating an electric field that enables high charge transport at the WO_3/WSe_2 heterostructure interface. The specific capacitance was evaluated for each electrode, as depicted in Figure S5a (Supporting Information). At 1 A g^{-1}, the WO_3/WSe_2-2 electrode exhibited a specific capacitance of 378.1 F g^{-1}, surpassing the values obtained for the WO_3/WSe_2-1 (298.63 F g^{-1}), WSe_2-3 (188.71 F g^{-1}), and WSe_2-4 (120.0 F g^{-1}) electrodes.

Furthermore, electrochemical impedance spectroscopy (EIS) measurements were performed to explore the redox kinetics of obtained materials. These measurements were performed for all electrodes at a fixed bias voltage of 10 mV. The results, depicted as Nyquist curves in Figure S5b (Supporting Information), which show nearly similar features characterized by a negligible semicircular arc at the high frequency and a sloped line at the low frequency. The intersection of the Nyquist plot with the real axis (Z') specifies the solution resistance (R_s), encompassing the internal resistance of active material, electrolyte resistance, and contact resistance of the electrode and electrolyte. The diameter of the semicircular arc along the real axis represents charge transfer resistance (R_{ct}), whereas the straight line along the imaginary axis signifies capacitive resistance. The R_s values calculated for WO_3/WSe_2-1, WO_3/WSe_2-2, WSe_2-3, and WSe_2-4 electrodes were 1.31, 0.75, 0.95, and 1.27 Ω, respectively. The low R_s for WO_3/WSe_2-2 indicate improved Na^+ ion accessibility of the active material, likely because of the existence of oxygen-based functional groups and enhanced charge-transfer kinetics at the heterointerface. The WO_3/WSe_2-1 and WO_3/WSe_2-2 electrodes show R_{ct} values of 3.45 and 1.46 Ω, respectively, while no obvious semicircular arc characteristic was observed in the Nyquist plot for WSe_2-3 and WSe_2-4 electrodes, suggesting negligible charge-transfer resistance.

The CV, GCD, and EIS results indicate the promising Na^+ ion storage capabilities of WO_3/WSe_2-2. Therefore, additional kinetic analyses were performed on this heterostructure to investigate rate performance and cycle life. Figure 5c (Figure S6, Supporting Information) demonstrates the CV curves of the WO_3/WSe_2-2 at different scanning rates. The rectangular outline remains consistent even at high rates of 100 mV s^{-1}, indicating rapid and reversible pseudocapacitive behavior. The charge storage mechanism was investigated by scrutinizing the relation between peak current (I) and scan rate (v) observed from CV profiles, using the power law equation,[41]

$$I = av^b \tag{5}$$

This analysis provides crucial insights into whether the charge storage is diffusion-controlled or non-diffusion-controlled.[42] In a diffusion-controlled process, capacitance mainly originates from faradaic reactions, resulting in a current response proportionate to a square root of the scan rate (b = 0.5). Conversely, in a non-diffusion-controlled capacitive process, capacitance arises from electric double-layer and surface pseudocapacitance, with a current response directly proportionate to the scan rate (b = 1). As revealed in Figure 5d, The calculated *b*-values for WO_3/WSe_2-1, WO_3/WSe_2-2, WSe_2-3, and WSe_2-4 electrodes were 0.85, 0.83, 0.87, and 0.81, respectively, indicating the dominance of charge storage contribution from a non-diffusion-controlled capacitive process. This could be ascribed to the sufficient accessibility for Na^+ ions facilitated by the ultrathin nanoflakes of the heterophase structure and a fully exposed wide interlayer surface of WSe_2. Besides, the total capacitance was divided into two categories: surface capacitive and diffusion-controlled. The surface capacitive percentage of WO_3/WSe_2-2 was calculated to be 56.7% at 5 mV s^{-1}, gradually increasing to 85.4% at 100 mV s^{-1} (Figure 5e), representing a dominated pseudocapacitance for the WO_3/WSe_2-2. Interestingly, a significant portion of the charge storage contribution in the WO_3/WSe_2-2 electrode arises from the non-diffusion-controlled capacitive charge storage mechanism. The shaded region in Figure S6e (Supporting Information) represents the diffusion-controlled charge storage of WO_3/WSe_2-2 at 60 mV s^{-1}, while the other region signifies capacitive charge storage. Overall, the kinetic study recommends that the maximum charge storage in WO_3/WSe_2-2 is capacitive across the entire scanning rates, indicating that the presence of duel WO_3 and WSe_2 phases, coupled with the heterostructure interface and expanded interlayer spacings, provide an optimal environment favorable for achieving high capacitive Na^+ ion storage.

The rate capability assessment of WO_3/WSe_2-2 heterostructures is evaluated through GCD measurements. Figure 5f (Figure S7, Supporting Information) illustrates the GCD curves of the WO_3/WSe_2-2 heterostructure at various current densities (1–20 A g^{-1}). The observed pseudocapacitive behavior in the charge–discharge traces defines the charge storage process of WO_3/WSe_2-2, distinct from the battery-type charge storage process. The WO_3/WSe_2-2 heterostructures displayed a maximum specific capacitance of 378.1 F g^{-1} at 1 A g^{-1} maintaining 64.7%

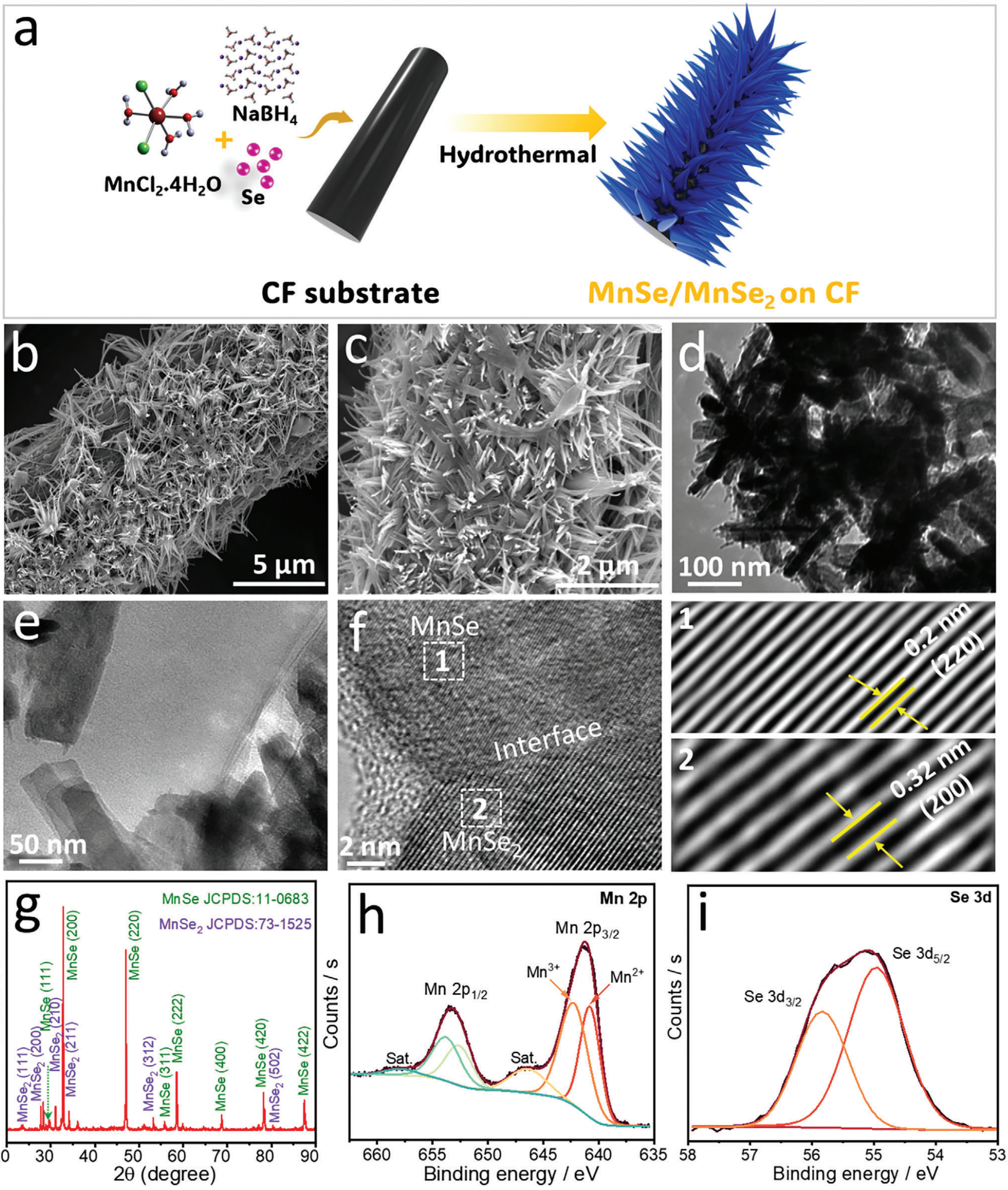

Figure 6. a) One-step growth protocol of the MnSe/$MnSe_2$ heterostructures on CF. b,c) low-and high-magnification SEM images of MnSe/$MnSe_2$ heterostructures, d–f) TEM and HRTEM images of MnSe/$MnSe_2$ heterostructures, indicating perfect interface between MnSe and $MnSe_2$, g) XRD pattern for MnSe/$MnSe_2$ heterostructures. XPS narrow scan spectra for h) Mn 2p and i) Se 3d of MnSe/$MnSe_2$ heterostructures.

(244.4 F g^{-1}) at 20 A g^{-1}, revealing excellent rate performance (Figure 5g). The rapid pseudocapacitive reactions gives an outstanding performance rate of WO_3/WSe_2-2, which is promising for ASIC. The specific capacitance of WO_3/WSe_2-2 was compared with earlier literature on TMDs-based electrodes as shown in Table S1 (Supporting Information). The metallic properties of WSe_2 and the presence of oxygen functional groups in WO_3/WSe_2-2 heterostructures on the surface and within the material are crucial for facilitating rapid Na^+ ions storage. Here, the heterostructure interface contributes to high electronic conductivity, while oxygen enhances ionic affinity, potentially increasing pseudocapacitance and Na^+ ions storage capacity.

As we know, electrodes with rapid redox kinetics and pseudocapacitive charge storage mechanisms exhibit minimal structural alterations during cycling. After 10000 GCD cycles at 10 A g^{-1}, the WO_3/WSe_2-2 heterostructures retained 95.0% of the initial capacitance, demonstrating excellent stability (Figure 5h). This outstanding cycling stability can be ascribed to a wide interspacing of WO_3/WSe_2-2 compared to the diameters of Na^+ ions, thereby accelerating Na^+ ion intercalation/deintercalation more proficiently, contributing to superior cycling stability. The WO_3/WSe_2-2 heterostructure comprises a 2D nanoarchitecture, wherein 2D nanosheets enhance redox-active sites and serve as an electron superhighway, mitigating interfacial resistance, as demonstrated in Figure 5i.

Moreover, to understand the reason behind the outstanding cycling stability and overall electrochemical performance of WO_3/WSe_2-2 during Na^+ ion storage, ex situ SEM, XRD, and XPS analyses were carried out. As shown in Figure S8 (Supporting Information), the ultrathin nanoflakes, which make the surface morphology of WO_3/WSe_2-2 preserved well, and the active material remains attached to the CF substrate even after repeated cycling, demonstrating the excellent cycling stability of the electrode. Moreover, the XRD data of WO_3/WSe_2-2 post-cycling (Figure S9a, Supporting Information) revealed no new impurities, except for a decline in (002) peak intensity corresponding to WSe_2 and a rise in the peak intensity of WO_3. The increase in oxygen content in the material after cycling in $NaClO_4$ aqueous electrolyte is likely due to a combination of surface oxidation of WO_3/WSe_2-2 exposed to the electrolyte, adsorption of oxygen species, and electrochemical processes taking place during the cycling process.[43]

The ex situ XPS spectra of WO_3/WSe_2-2 offer detailed insights into the redox process during Na^+ ion storage. The comparative survey scan spectra of WO_3/WSe_2-2 before and after cycling are depicted in Figure S9b (Supporting Information). The presence of Na 1s is evident in the material due to the repetitive insertion and extraction of Na^+ ions during cycling, underscoring the robust Na^+ ion storage properties of WO_3/WSe_2-2 (Figure S9c, Supporting Information). The high-resolution O 1s spectrum (Figure S9d, Supporting Information) of WO_3/WSe_2-2 post-cycling reveals an additional peak at 533.2 eV corresponding to the surface hydroxyl (W-OH) group. Furthermore, the high-resolution W 4f spectrum primarily displays two states of W, as depicted in Figure S9e (Supporting Information). While most peaks corresponding to W $4f_{7/2}$ and W $4f_{5/2}$ species in WSe_2 exhibit no significant change post-cycling, the intensity of W $4f_{7/2}$ and W $4f_{5/2}$ of WO_3 related to W^{6+} states increase. Oxygen-containing species from the electrolyte can adsorb onto the surface of WSe_2 during cycling. This adsorption can lead to the incorporation of oxygen into the WSe_2 lattice or forming surface oxides. Conversely, the Se 3d spectrum (Figure S9f, Supporting Information) after cycling shows no noticeable change, and notably, there is no formation of SeO_x compounds post-cycling, indicating exceptional structural stability.[20]

The systematic electrochemical investigations reveal that the outstanding Na^+ ion storage performance is attributed to the newly constructed diphasic WO_3/WSe_2 heterostructures, along with four key factors: i) The introduction of defective regions at the heterojunction interface facilitates Na^+ ion diffusion and electron conduction efficiently. ii) The strong bonding at the heterojunction interface enhances mechanical stability. iii) The heterostructure creates an inherent electric field, expediting ion transfer and minimizing the diffusion barrier for Na^+ ions, thereby enhancing rate capability and Na^+ ion storage performance and iv) The direct growth of the WO_3/WSe_2-2 on CF facilitates the facile access of Na^+ ions. Therefore, the WO_3/WSe_2-2 heterostructure demonstrates excellent sodium ion storage performance.

2.3. Characterization and Na^+ Ion Storage Performance of $MnSe/MnSe_2$ Heterostructures

The fabrication of hierarchical $MnSe/MnSe_2$ nanowires on a CF substrate was successfully achieved over a controlled one-step hydrothermal process, as illustrated in **Figure 6a**. The morphology and microstructural details of the $MnSe/MnSe_2$ were examined through SEM and TEM, as depicted in Figure 6b-i. The prepared $MnSe/MnSe_2$ sample exhibited a nanowire-like morphology with a length extending several micrometers and lateral dimensions of 20–30 nm (Figure 6b,c), growing vertically on the CF substrate. SEM-EDS mappings confirmed the consistent dispersal of Mn and Se elements (Figure S10, Supporting Information). Further characterization of the nanowire-like morphology of $MnSe/MnSe_2$ was conducted using TEM, as depicted in Figure 6d,e. The HRTEM image in Figure 6f delineates the heterostructure boundary. Lattice fringes with d-spacings of 0.2 and 0.32 nm were seen in the HRTEM image of $MnSe/MnSe_2$, equivalent to the (220) and (200) planes of MnSe and $MnSe_2$, respectively.[44]

Figure 6g depicts the XRD pattern of $MnSe/MnSe_2$, revealing sharp and intense diffraction peaks indicative of highly crystalline material formation. Notably, strong diffraction peaks observed at 32.9°, 47.1°, 55.9°, 68.8°, 78.4°, and 87.5° correspond to the (200), (220), (311), (222), (400), (420), and (422) planes, respectively, of the cubic MnSe phase (JCPDS no. 11-0683).[45] Additionally, small diffraction peaks from the tetragonal $MnSe_2$ phase (JCPDS no. 73-1525) were noted at 27.9°, 30.8°, 34.1°, and 53.4°, corresponding to the (200), (210), (211), and (312) planes.[44] These findings confirm the successful formation of manganese selenide with well-defined crystalline phases. Moreover, XPS analysis provided insights into the oxidation states and elemental composition of $MnSe/MnSe_2$. The survey scan spectrum (Figure S10h, Supporting Information) confirmed the occurrence of Mn and Se elements at their respective binding energies. Additionally, peaks attributed to C 1s (from the CF substrate and reference) and O 1s were observed, likely stemming from surface contamination upon exposure to air. Further characterization of oxidation states and element-binding was achieved through narrow-scan spectra. The Mn 2p spectrum (Figure 6h) displayed two prominent peaks matching to Mn $2p_{3/2}$ and Mn $2p_{1/2}$ levels. The Mn $2p_{3/2}$ peaks at 640.7 and 642.3 eV match the Mn^{2+} and Mn^{3+} oxidation states, respectively.[44] The existence of Mn^{2+} species was supported by shake-up satellite peaks, which are generally absent for Mn^{3+} and Mn^{4+} states.[45] The Se 3d spectrum (Figure 6i) exhibited a spin-orbit doublet centered at 54.9 and 56.1 eV for Se $3d_{5/2}$ and Se $3d_{3/2}$, respectively. Notably, no peaks corresponding to zero-valent Se (55.1 eV) or oxidized SeO_x species (≈59 eV) were detected in the spectrum.

Furthermore, the electrochemical features of the MnSe/$MnSe_2$ heterostructure were assessed in a three-electrode setup using a 2 м $NaClO_4$ aqueous solution. Figure S11a (Supporting Information) illustrates the CV profiles of MnSe/$MnSe_2$ at 5 to 100 mV s^{-1}, within an operational potential range of 0–1.0 V versus SCE. The CV displays a distorted rectangular outline, signifying reversible Na^+ ion intercalation/deintercalation into the electrode material. Additionally, the *b*-value for the cathodic region of the MnSe/$MnSe_2$ electrode was determined to be 0.85 (Figure S11b, Supporting Information), suggesting that the reaction current originates from the surface capacitive charge storage process. This finding implies that MnSe/$MnSe_2$ nanowires reduce the transport paths for electrolyte ions and enhance electrolyte accessibility to the surface active sites, thereby favoring a surface capacitive-controlled charge storage contribution. As shown in Figure S11c (Supporting Information), the GCD of MnSe/$MnSe_2$ recorded at different current densities exhibit an almost symmetric triangular outline, indicative of high redox reversibility. At a current density of 1 A g^{-1}, MnSe/$MnSe_2$ electrode achieved a specific capacitance of 445.8 F g^{-1}. Even at 20 A g^{-1}, the electrode retained 68.6% of its initial capacitance (Figure S11d, Supporting Information). Notably, this specific capacitance exceeds that reported for earlier flower-like MnSe (123.1 F g^{-1} at 1 A g^{-1}),[46] α-MnSe nanoparticles (96.76 F g^{-1} at 0.1 mA cm^{-2}),[47] and cube-like $MnSe_2$ (50.79 F g^{-1}).[48] The EIS measurements of MnSe/$MnSe_2$ heterostructures reveal the R_s and R_{ct} values of 1.77 and 2.35 Ω, respectively (Figure S10e, Supporting Information). Furthermore, the cyclic stability of the MnSe/$MnSe_2$ was evaluated through continuous GCD at 10 A g^{-1} for 10 000 cycles. Figure S10f (Supporting Information) illustrates that the MnSe/$MnSe_2$ heterostructures retained 91.3% of their initial value after the cycling test, exhibiting a retention rate higher than other manganese-based electrodes. Additionally, the MnSe/$MnSe_2$ electrode exhibited 100% Coulombic efficiency throughout the cycling tests. The electrochemical characteristics observed in the MnSe/$MnSe_2$ electrode indeed suggest its promising potential for Na^+ ion storage. Overall, the results obtained for both the MnSe/$MnSe_2$ electrode and WO_3/WSe_2-2 indicate that the active materials and electrodes are robust, rendering them suitable for application in sodium-based energy storage systems.

2.4. Application in Aqueous Sodium-Ion Capacitor (ASIC) System

A compelling demonstration of the high Na^+ ions storage capability and long-lasting cycling stability of WO_3/WSe_2-2 anode, along with MnSe/$MnSe_2$ cathode, both dual-heterostructure electrodes, results in a curious assembly of ASIC cell that could meet the requirements of competent energy storage systems. The main objective of employing WO_3/WSe_2-2, and MnSe/$MnSe_2$ electrodes is to expand system voltage and combine characteristics of pseudocapacitive materials within individual cells for Na^+ ion storage. Therefore, integrating them in ASIC cells could directly enhance the energy storage capacity and the systems overall performance. Both electrodes in the ASIC system are separated by a Whatman filter paper and an aqueous 2 м $NaClO_4$ electrolyte, as shown in a schematic illustration of the assembled ASIC cell (**Figure 7a**). Considering the specific capacitance of the MnSe/$MnSe_2$ and WO_3/WSe_2-2, the ASIC cell was constructed with a positive electrode: negative electrode mass ratio of 1.0:1.2. The operating voltage of the MnSe/$MnSe_2$//WO_3/WSe_2-2 ASIC cell is estimated to be 0–2.0 V based on the circumstance that the positive side potential range of the MnSe/$MnSe_2$ electrode is from 0 to 1.0 V, whereas the negative side potential range of the WO_3/WSe_2-2 electrode varies from −1.0 to 0 V (Figure 7b). To validate the suitable operating potential window, the MnSe/$MnSe_2$//WO_3/WSe_2-2 ASIC cell endured testing across various cell voltage ranges using CV and GCD measurements. Figure S12a,b (Supporting Information) depicts the CV and GCD profiles of the MnSe/$MnSe_2$//WO_3/WSe_2-2 ASIC cell under different cell voltages. Notably, even at high cell voltage (0–2.0 V), the MnSe/$MnSe_2$//WO_3/WSe_2-2 ASIC cell exhibited minimal polarization in both CV and GCD curves, indicating a combined energy storage mechanism from the redox active sites of the pseudocapacitive materials. Therefore, the operating cell voltage was fixed at 0–2.0 V, and subsequent CV and GCD tests were performed at various scan rates and current densities to evaluate rate performance.

Figure 7c displays CV profiles of the MnSe/$MnSe_2$//WO_3/WSe_2-2 ASIC at 5–100 mV s^{-1} in an operating voltage window of 0–2.0 V. Regardless of the scan rate, CV profiles maintained a quasi-rectangular outline, featuring prominent redox peaks with pseudocapacitive characteristics, indicating good reversibility and redox kinetics of the cell. Further GCD analysis at different current densities (Figure 7d) demonstrated nearly triangular features. The calculated specific capacitance of MnSe/$MnSe_2$//WO_3/WSe_2-2 ASIC cell from the discharge time are 147.7, 130.8, 122.0, 115.8, 1.08.2, 105.8, 100.9, 98.3, and 96.0 F g^{-1} at 2, 4, 6, 8, 10, 12, 14, 16, 18, and 20 A g^{-1}, respectively, as depicted in Figure 7e. Notably, the cell exhibited superior rate capability, with a 65% retention rate at 20 A g^{-1}, validating its outstanding mass balancing and Na^+ ion storage properties. Additionally, the energy density and power density values of the MnSe/$MnSe_2$//WO_3/WSe_2-2 ASIC cell were evaluated to assess practical application viability. The Ragon plot (Figure 7f) revealed a maximum energy density of 82.1 Wh kg^{-1} at a power density of 1873.5 W kg^{-1} and a retention of 53.3 Wh kg^{-1} at a high power density of 18 735.4 W kg^{-1}. These values notably surpass those reported for hybrid SCs based on TMDs, such as $MoSe_2$@ WSe_2//$MoSe_2$@ WSe_2 (14.44 Wh kg^{-1} at 397 W kg^{-1}),[49] WSe_2//AC (25.5 Wh kg^{-1} at 1111 W kg^{-1}),[50] $MoSe_2$//$MoSe_2$ (36.2 Wh kg^{-1} at 1400 W kg^{-1}),[51] Ti_3C_2//WS_2 (50.8 Wh kg^{-1} at 813.6 W kg^{-1}),[52] 1T-WSe_2/graphene//N-doping Gra (75.63 Wh kg^{-1} at 375 W kg^{-1}),[53] WS_2@Ni-Co-S//rose carbon (40.01 Wh kg^{-1} at

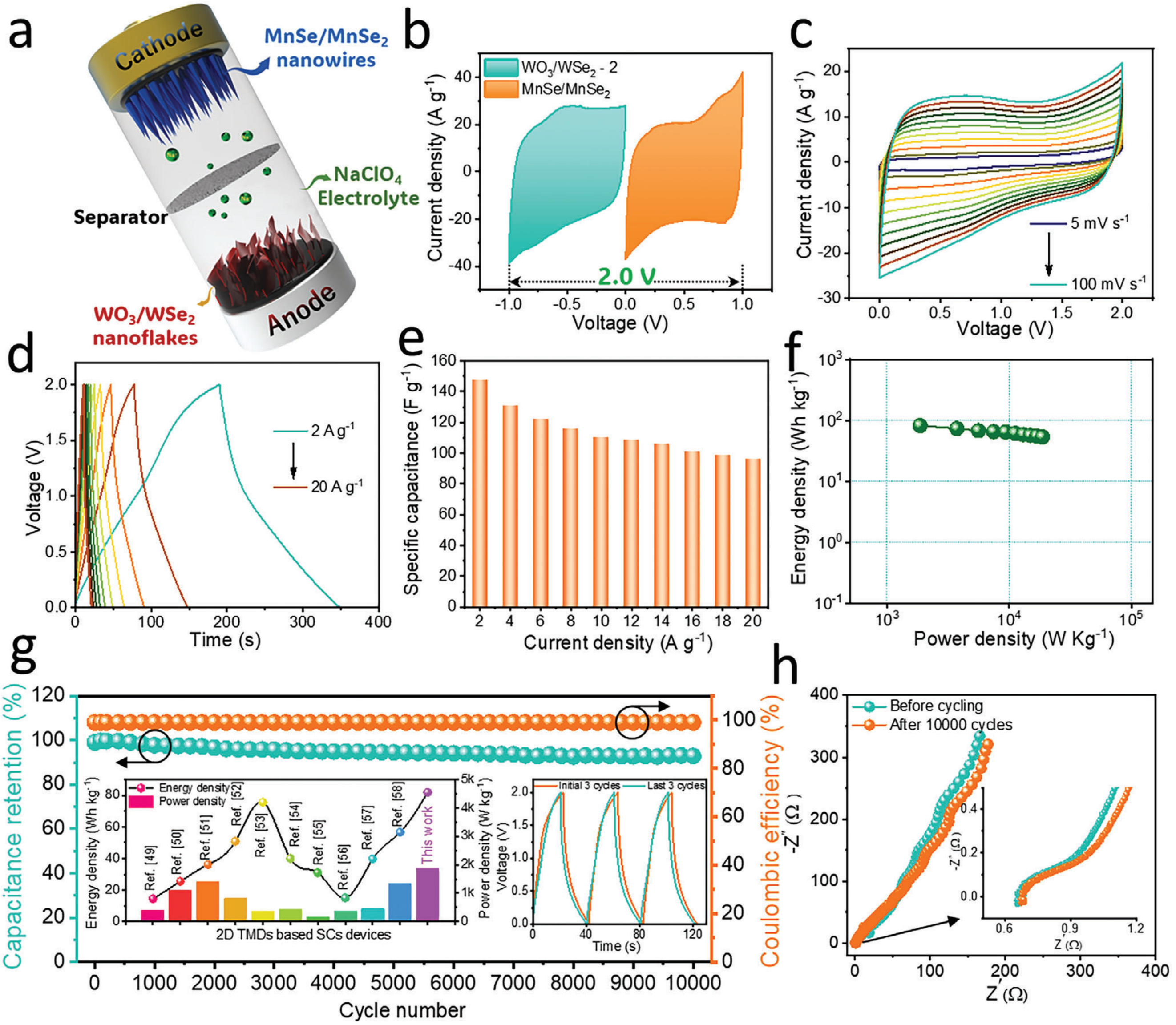

Figure 7. a) Schematics illustration for the assembled MnSe/$MnSe_2$//WO_3/WSe_2-2 ASIC cell. b) CV curves of the WO_3/WSe_2-2 and MnSe/$MnSe_2$ heterostructures measured at a scan rate of 100 mV s^{-1}, indicating possible cell voltage of 2.0 V. c) CV and d) GCD curves of the MnSe/$MnSe_2$//WO_3/WSe_2-2 ASIC cell measured at different scan rates and current densities, respectively, e) calculated specific capacitance concerning the applied current density. f) Ragon plot and g) cycling stability (Coulombic efficiency) concerning cycle number of the MnSe/$MnSe_2$//WO_3/WSe_2-2 ASIC cell. The inset of g) shows the comparative energy and power densities of the ASIC cell with previously reported work and GCD profiles of the initial and last three cycles of the ASIC cell, and h) Nyquist plot of the fabricated ASIC cell before and after cycling stability measurements, respectively.

417.52 W kg^{-1}),[54] MoS_2/NiS//AC (31 Wh kg^{-1} at 155.7 W kg^{-1}),[55] rGO/MoS_2/WS_2//rGO (15 Wh kg^{-1} at 373 W kg^{-1}),[56] 1T-2H-O MoS_2//MnO_2 (39.7 Wh kg^{-1} at 450 W kg^{-1}),[57] WS_2/WO_3//AC (56.6 Wh kg^{-1} at 1335 W kg^{-1}).[58] The comprehensive analysis of our MnSe/$MnSe_2$//WO_3/WSe_2-2 ASIC cell with previous research is presented in the inset of Figure 7g and Table S2 (Supporting Information). The results prove that the MnSe/$MnSe_2$//WO_3/WSe_2-2 ASIC cell is a competent energy storage cell with both high power and energy density. The cyclic stability of the MnSe/$MnSe_2$//WO_3/WSe_2-2 ASIC cell was further examined to evaluate its durability over continuous GCD cycles. The cycling stability test was conducted at 10 A g^{-1} over 10 000 cycles, as illustrated in Figure 7g. The cell exhibited impressive capacity retention of 92.9% alongside an admirable Coulombic efficiency of 94.6%, indicating its robust cycling performance. The GCD profiles of the initial and last three cycles of the ASIC cell indicate a slight decrease in discharge time after 10000 cycles, suggesting high cycling stability. Additionally, the EIS plot before and after cycling demonstrates a lower charge transfer resistance of the ASIC cell, suggesting favorable ionic and electrochemical kinetics (Figure 7h).

The Na^+ ion storage mechanism of the ASIC full cell was further evaluated using ex situ SEM and XPS analyses at various charge/discharge states during the second cycle. The

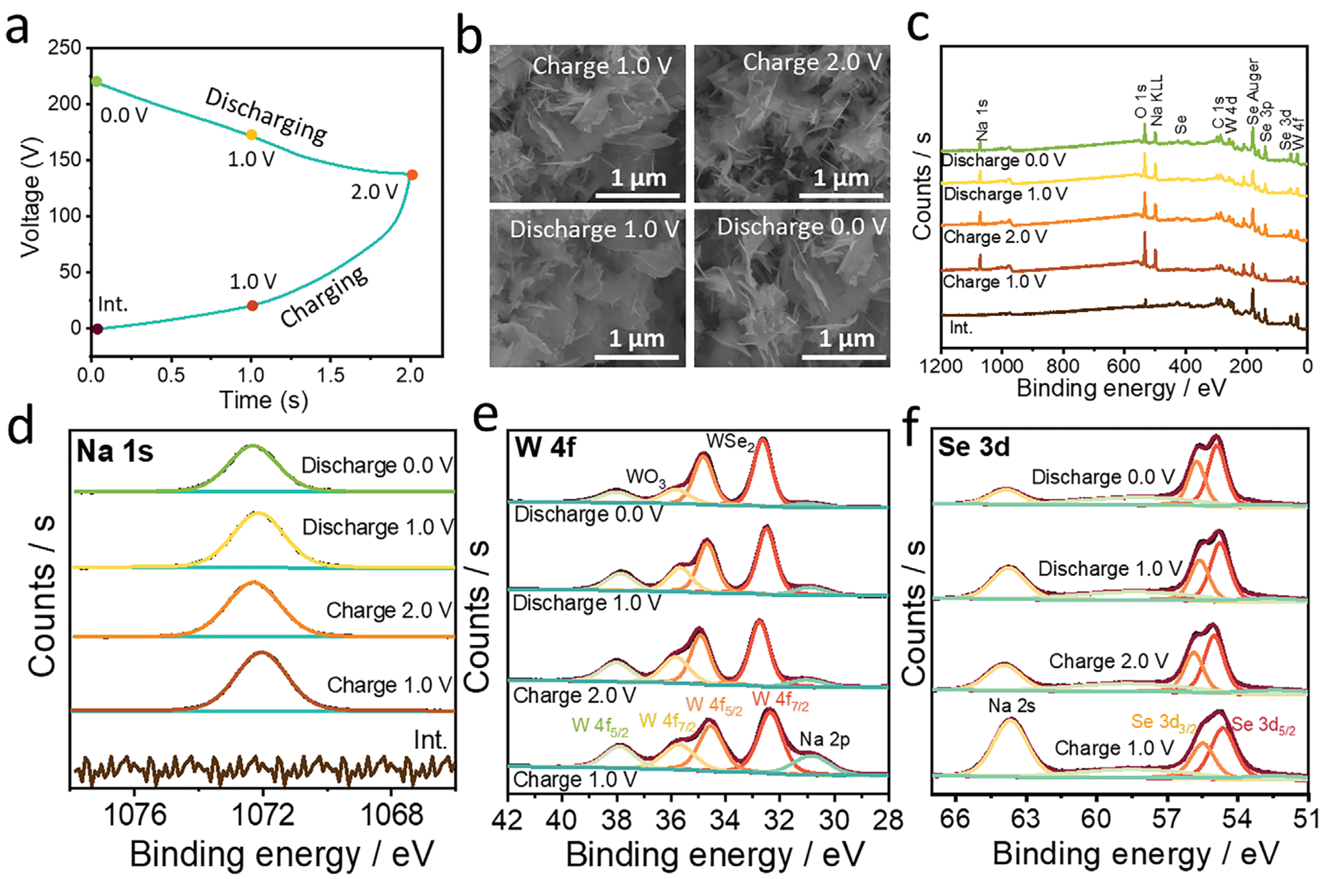

Figure 8. a) Different charge/discharge states point on the GCD profiles of ASIC, b) Ex situ SEM images of WO_3/WSe_2-2 anode at different charge/discharge states, c) Ex situ XPS survey scan spectra of WO_3/WSe_2-2 anode. Ex situ study of the high-resolution d) Na 1s, e) W 4f, and f) Se 3d of WO_3/WSe_2-2 anode.

corresponding discharge/charge states are marked in the GCD profile (**Figure** 8a). The morphology of the WO_3/WSe_2-2 anode did not change significantly during the charging process. However, in a fully charged state, small nanoparticles appeared on the WO_3/WSe_2-2 nanosheets, indicating Na^+ ion intercalation. Surprisingly, even after full discharge, the nanoflake morphology was well maintained (Figure 8b). The XPS survey scan spectra of the WO_3/WSe_2-2 anode at various charge/discharge states are presented in Figure 8c, confirming the presence of Na 1s along with the main elements of WO_3/WSe_2-2, including W, Se, O, and C. Figure 8d shows the high-resolution Na 1s XPS spectra of the WO_3/WSe_2-2 at different charge and discharge stages. As illustrated, no Na 1s signal was detected in the initial state of the WO_3/WSe_2-2 electrode, whereas a broad peak is observed at different charge and discharge states, demonstrating the insertion of Na^+ ions into the WO_3/WSe_2-2 nanosheets. Moreover, the typical Na peak shifts to higher binding energies during the charging process and returns to the original position after full discharge, indicating the excellent reversibility of Na^+ intercalation and deintercalation in the WO_3/WSe_2-2 electrode.[59] Notably, even after full discharge, a small number of trapped Na^+ ions in the electrode might serve as interlayer pillars, further stabilizing the layered structure of the WO_3/WSe_2-2 nanosheets during electrochemical cycling. The W 4f XPS spectra of the WO_3/WSe_2-2 anode at different charge/discharge states are presented in Figure 8e. The main doublet peaks of W^{4+} in 2H WSe_2 are located at 32.5 and 34.7 eV, and other low-intensity doublet peaks at 35.6 and 37.7 eV are related to $4f_{7/2}$ and $4f_{5/2}$ of WO_3, respectively. As seen in the spectra, a slight shift in binding energy was observed in the fully charged state.[60] In the fully discharged state, the peaks shifted toward the original state, confirming the insertion and extraction of Na^+ ions during the charge/discharge process. However, it can be observed that the peak intensity of the fully charged 2H WSe_2 is significantly higher than that of WO_3, which also proves that the intercalation of Na^+ ions increases the interlayer distance which stabilizes the WSe_2 phase from oxidation. The peak corresponding to Na 2p is located at 30.8 eV alongside the W $4f_{7/2}$ of 2H WSe_2. The intensity of Na 2p is higher in the first charging state, whereas it decreases in the fully discharged state.

Meanwhile, the XPS spectra of Se 3d show negligible variation at all representative charge/discharge states, further indicating that the Se element has a limited contribution to the electrochemical reaction. A slight shift toward higher binding energy upon charging and return to their original positions after discharging was observed, whereas no features of SeOx were seen. The peak located at 63.6 eV is related to Na 2s. Overall, the shifting and diminished intensities of the peaks in the elemental spectra upon charging support the insertion of Na^+ ions. These results indicate that Na^+ ions were inserted into and extracted from the WO_3/WSe_2-2 anode during the charging and discharging process.[61]

The findings suggest that the WO_3/WSe_2-2 anode shows significant promise for Na^+ ion storage. The presence of WSe_2 enhances the overall conductivity of the heterostructure optimizing charge transport efficiency. The interlayer spacing of WSe_2 facilitates the smooth insertion and extraction of ions, thereby increasing the Na^+ ion storage capacity. Additionally, the heterostructure boosts the specific surface area, offering numerous active sites for Na^+ ion interaction. The oxygen component in the material further enhances surface interactions, forming hydrogen bonds that contribute to charge storage. This dynamic process of strong bond formation electronic coupling in WO_3 and WSe_2 leads to effective Na^+ ion storage in the WO_3/WSe_2-2 anode, while the improved interlayer spacing enhances the overall storage capacity of the device. The obtained data demonstrates that our proposed $MnSe/MnSe_2//WO_3/WSe_2$-2 cell and its resulting Na^+ ions storage performance represent a pioneering advancement toward achieving superior energy storage capabilities suitable for practical applications.

3. Conclusion

In summary, the atomically thin 2D nanosheets of WO_3/WSe_2 heterostructures were successfully synthesized via a scalable yet simple hydrothermal method followed by the chemical vapor deposition (CVD) directly on the carbon fiber (CF) substrate for efficient Na^+ ion storage. The heterostructure exhibits wide interlayer spacings that are favorable for storing large Na^+ ions and improve electronic conductivity. Density functional theory (DFT) calculations corroborate these findings, elucidating the superior electrochemical performance of WO_3/WSe_2 heterostructures, primarily attributed to charge transfer from the O-atoms of WO_3 to the W-5d and Se-4p-orbitals of the WSe_2 (002) surface. As a result, the WO_3/WSe_2 electrode demonstrates exceptional Na^+ ion storage features, with a specific capacitance of 378.1 F g^{-1} at 1 A g^{-1}, excellent rate performance, and long-lasting cycling stability over 10 000 cycles. The ASIC cell comprising WO_3/WSe_2 as the negative electrode and $MnSe/MnSe_2$ as the positive electrode achieved a peak energy density of 82.1 Wh kg^{-1} at a power density of 1873.5 W kg^{-1}, along with high rate performance and long-cycle stability. Our work presents a simplistic and useful approach to overcome the sluggish Na^+ ion and redox kinetics of layered TMDs. We accomplish this by introducing a specific heterointerface that enables fast ion diffusion and forms a conductive system for effective electron transfer. We believe that the insights from the present work pave the technique for rational design and optimization of the interfacial electronic features in 2D heterostructures for next-generation ASIC, enabling high energy and power densities.

Supporting Information

Supporting Information is available from the Wiley Online Library or from the author.

Acknowledgements

This work was supported by the Japan Society for the Promotion of Science (JSPS) KAKENHI Grant Number JP22F22368, JP20H00392, and JP23H05459. A part of this work was supported by "Advanced Research Infrastructure for Materials and Nanotechnology in Japan (ARIM)" of the Ministry of Education, Culture, Sports, Science and Technology (MEXT). Proposal Number JPMXP1224NM5281.

Conflict of Interest

The authors declare no conflict of interest.

Data Availability Statement

The data that support the findings of this study are available in the supplementary material of this article.

Keywords

aqueous system, energy storage, heterostructures, Na ion capacitor

Received: April 14, 2024
Revised: June 6, 2024
Published online: July 3, 2024

---

[1] a) S. Fleischmann, J. B. Mitchell, R. Wang, C. Zhan, D.-e. Jiang, V. Presser, V. Augustyn, *Chem. Rev.* **2020**, *120*, 6738; b) X. Wang, X. Lu, B. Liu, D. Chen, Y. Tong, G. Shen, *Adv. Mater.* **2014**, *26*, 4763.
[2] a) C. Liu, F. Li, L. P. Ma, H. M. Cheng, *Adv. Mater.* **2010**, *22*, E28; b) Z. Zhu, T. Jiang, M. Ali, Y. Meng, Y. Jin, Y. Cui, W. Chen, *Chem. Rev.* **2022**, *122*, 16610.
[3] a) R. Stephanie, C. Y. Park, P. A. Shinde, E. Alhajri, N. R. Chodankar, T. J. Park, *Energy Storage Mater.* **2024**, *68*, 103336; b) L. Dong, W. Yang, W. Yang, C. Wang, Y. Li, C. Xu, S. Wan, F. He, F. Kang, G. Wang, *Nano-Micro Lett.* **2019**, *11*, 94.
[4] J. Ding, W. Hu, E. Paek, D. Mitlin, *Chem. Rev.* **2018**, *118*, 6457.
[5] S. Wang, Q. Wang, W. Zeng, M. Wang, L. Ruan, Y. Ma, *Nano-Micro Lett.* **2019**, *11*, 70.
[6] a) P. A. Shinde, N. R. Chodankar, H.-J. Kim, M. A. Abdelkareem, A. A. Ghaferi, Y.-K. Han, A. G. Olabi, K. Ariga, *ACS Energy Lett.* **2023**, *8*, 4474; b) S. Manzeli, D. Ovchinnikov, D. Pasquier, O. V. Yazyev, A. Kis, *Nat. Rev. Mater.* **2017**, *2*, 17033.
[7] M. H. Han, E. Gonzalo, G. Singh, T. Rojo, *Energy Environ. Sci.* **2015**, *8*, 81.
[8] a) X. Wu, H. Zhang, J. Zhang, X. W. Lou, *Adv. Mater.* **2021**, *33*, 2008376; b) G. R. Bhimanapati, Z. Lin, V. Meunier, Y. Jung, J. Cha, S. Das, D. Xiao, Y. Son, M. S. Strano, V. R. Cooper, L. Liang, S. G. Louie, E. Ringe, W. Zhou, S. S. Kim, R. R. Naik, B. G. Sumpter, H. Terrones, F. Xia, Y. Wang, J. Zhu, D. Akinwande, N. Alem, J. A. Schuller, R. E. Schaak, M. Terrones, J. A. Robinson, *ACS Nano* **2015**, *9*, 11509.
[9] D. Voiry, A. Mohite, M. Chhowalla, *Chem. Soc. Rev.* **2015**, *44*, 2702.
[10] Q. Fu, J. Han, X. Wang, P. Xu, T. Yao, J. Zhong, W. Zhong, S. Liu, T. Gao, Z. Zhang, *Adv. Mater.* **2021**, *33*, 1907818.
[11] M. Chhowalla, H. S. Shin, G. Eda, L.-J. Li, K. P. Loh, H. Zhang, *Nat. Chem.* **2013**, *5*, 263.
[12] T. Lu, S. Dong, C. Zhang, L. Zhang, G. Cui, *Coord. Chem. Rev.* **2017**, *332*, 75.
[13] a) G. Tang, J. Liang, W. Wu, *Adv. Funct. Mater.* **2024**, *34*, 2310399; b) I. Hussain, S. Sahoo, C. Lamiel, T. T. Nguyen, M. Ahmed, C. Xi, S. Iqbal,

A. Ali, N. Abbas, M. S. Javed, *Energy Storage Mater.* **2022**, *47*, 13; c) P. A. Shinde, N. R. Chodankar, M. A. Abdelkareem, S. J. Patil, Y.-K. Han, K. Elsaid, A. G. Olabi, *Small* **2022**, *18*, 2200248.
[14] a) H. Li, J. Wu, Z. Yin, H. Zhang, *Acc. Chem. Res.* **2014**, *47*, 1067; b) J.-K. Huang, J. Pu, C.-L. Hsu, M.-H. Chiu, Z.-Y. Juang, Y.-H. Chang, W.-H. Chang, Y. Iwasa, T. Takenobu, L.-J. Li, *ACS Nano* **2014**, *8*, 923.
[15] a) P. A. Shinde, K. Ariga, *Langmuir* **2023**, *39*, 18175; b) K. Ariga, *Bull. Chem. Soc. Jpn.* **2023**, *2*, 2200113; c) P. A. Shinde, A. G. Olabi, N. R. Chodankar, S. J. Patil, S.-K. Hwang, M. A. Abdelkareem, *Chem. Eng. J.* **2023**, *454*, 140246.
[16] M. Ishii, Y. Yamashita, S. Watanabe, K. Ariga, J. Takeya, *Nature* **2023**, *622*, 285.
[17] a) T. W. Lin, T. Sadhasivam, A. Y. Wang, T. Y. Chen, J. Y. Lin, L. D. Shao, *ChemElectroChem* **2018**, *5*, 1024; b) L. Lin, W. Lei, S. Zhang, Y. Liu, G. G. Wallace, J. Chen, *Energy Storage Mater.* **2019**, *19*, 408.
[18] N. Choudhary, C. Li, H.-S. Chung, J. Moore, J. Thomas, Y. Jung, *ACS Nano* **2016**, *10*, 10726.
[19] J. R. Xavier, R. B. J., *J. Alloys Compd.* **2023**, *947*, 169483.
[20] X. Zhao, H.-E. Wang, Y. Yang, Z. G. Neale, R. C. Massé, J. Cao, W. Cai, J. Sui, G. Cao, *Energy Storage Mater.* **2018**, *12*, 241.
[21] M. Shao, H. Sheng, L. Lin, H. Ma, Q. Wang, J. Yuan, X. Zhang, G. Chen, W. Li, Q. Su, E. Xie, J. Wang, Z. Zhang, W. Lan, *Small* **2023**, *19*, 2205529.
[22] Z. Dong, X. Wu, M. Chen, H. Chen, K.-J. Huang, L. Wang, J. Xu, *J. Colloid Interface Sci.* **2023**, *630*, 426.
[23] X. Feng, M. Xia, J. Ning, D. Wang, *ACS Appl. Energy Mater.* **2023**, *6*, 6391.
[24] P. A. Shinde, A. C. Lokhande, N. R. Chodankar, A. M. Patil, J. H. Kim, C. D. Lokhande, *Electrochim. Acta* **2017**, *224*, 397.
[25] a) L. Xing, K. Han, Q. Liu, Z. Liu, J. Chu, L. Zhang, X. Ma, Y. Bao, P. Li, W. Wang, *Energy Storage Mater.* **2021**, *36*, 309; b) X. Wu, S. Yao, *Nano Energy* **2017**, *42*, 143.
[26] B. Liu, T. Luo, G. Mu, X. Wang, D. Chen, G. Shen, *ACS Nano* **2013**, *7*, 8051.
[27] G. Zhang, X. Ou, J. Yang, Y. Tang, *Small Methods* **2021**, *5*, 2100374.
[28] S. Bandi, A. K. Srivastav, *CrystEngComm* **2021**, *23*, 1821.
[29] L. Xing, K. Han, Q. Liu, Z. Liu, J. Chu, L. Zhang, X. Ma, Y. Bao, P. Li, W. A. Wang, *Energy Storage Mater.* **2021**, *36*, 309.
[30] R. Rosati, I. Paradisanos, L. Huang, Z. Gan, A. George, K. Watanabe, T. Taniguchi, L. Lombez, P. Renucci, A. Turchanin, B. Urbaszek, E. Malic, *Nat. Commun.* **2023**, *14*, 2438.
[31] S. Wang, H. Chen, G. Gao, T. Butburee, M. Lyu, S. Thaweesak, J.-H. Yun, A. Du, G. Liu, L. Wang, *Nano Energy* **2016**, *24*, 94.
[32] P. A. Shinde, Y. Seo, C. Ray, S. C. Jun, *Electrochim. Acta* **2019**, *308*, 231.
[33] R. Addou, R. M. Wallace, *ACS Appl. Mater. Interfaces* **2016**, *8*, 26400.
[34] Q. Lv, J. Tan, Z. Wang, P. Gu, H. Liu, L. Yu, Y. Wei, L. Gan, B. Liu, J. Li, F. Kang, H.-M. Cheng, Q. Xiong, R. Lv, *Nat. Commun.* **2023**, *14*, 2717.
[35] B.-Q. Zhang, J.-S. Chen, H.-L. Niu, C.-J. Mao, J.-M. Song, *Nanoscale* **2018**, *10*, 20266.
[36] Y.-C. Lin, B. Jariwala, B. M. Bersch, K. Xu, Y. Nie, B. Wang, S. M. Eichfeld, X. Zhang, T. H. Choudhury, Y. Pan, R. Addou, C. M. Smyth, J. Li, K. Zhang, M. A. Haque, S. Fölsch, R. M. Feenstra, R. M. Wallace, K. Cho, S. K. Fullerton-Shirey, J. M. Redwing, J. A. Robinson, *ACS Nano* **2018**, *12*, 965.
[37] Q. Lv, J. Tan, Z. Wang, P. Gu, H. Liu, L. Yu, Y. Wei, L. Gan, B. Liu, J. Li, *Nat. Commun.* **2023**, *14*, 2717.
[38] R. Diehl, G. Brandt, E. Salje, *Acta Cryst. B* **1978**, *34*, 1105.
[39] W. Tang, E. Sanville, G. Henkelman, *J. Phys.: Condens. Matter* **2009**, *21*, 084204.
[40] K. Qian, L. Li, D. Yang, B. Wang, H. Wang, G. Yuan, J. Bai, S. Ma, G. Wang, *Adv. Funct. Mater.* **2023**, *33*, 2213009.
[41] P. A. Shinde, Y. Seo, S. Lee, H. Kim, Q. N. Pham, Y. Won, S. Chan Jun, *Chem. Eng. J.* **2020**, *387*, 122982.
[42] X. Wang, T. S. Mathis, K. Li, Z. Lin, L. Vlcek, T. Torita, N. C. Osti, C. Hatter, P. Urbankowski, A. Sarycheva, *Nat. Energy* **2019**, *4*, 241.
[43] a) L. Kang, S. Liu, Q. Zhang, J. Zou, J. Ai, D. Qiao, W. Zhong, Y. Liu, S. C. Jun, Y. Yamauchi, J. Zhang, *ACS Nano* **2024**, *18*, 2149; b) X.-Z. Zhai, J. Qu, S.-M. Hao, Y.-Q. Jing, W. Chang, J. Wang, W. Li, Y. Abdelkrim, H. Yuan, Z.-Z. Yu, *Nano-Micro Lett.* **2020**, *12*, 56.
[44] L. Hu, L. Cao, L. Li, J. Duan, X. Liao, F. Long, J. Zhou, Y. Xiao, Y.-J. Zeng, S. Zhou, *Mater. Horiz.* **2021**, *8*, 1286.
[45] H. Tang, Y. Yuan, L. Meng, W. Wang, J. Lu, Y. Zeng, T. Huang, C. Gao, *Adv. Mater. Technol.* **2018**, *3*, 1800074.
[46] H. Duan, S. Wang, B. Li, S. Ma, *New J. Chem.* **2023**, *47*, 8297.
[47] S. Sahoo, P. Pazhamalai, K. Krishnamoorthy, S.-J. Kim, *Electrochim. Acta* **2018**, *268*, 403.
[48] M. Pathak, D. Tamang, M. Kandasamy, B. Chakraborty, C. S. Rout, *Appl. Mater. Today* **2020**, *19*, 100568.
[49] A. B. Patel, J. V. Vaghasiya, P. Chauhan, C. Sumesh, V. Patel, S. S. Soni, K. D. Patel, P. Garg, G. K. Solanki, V. M. Pathak, *Nanoscale* **2022**, *14*, 6636.
[50] D. Singh, A. Singh, S. K. Ojha, A. K. Ojha, *Synth. Met.* **2023**, *293*, 117263.
[51] Y. Qiu, X. Li, M. Bai, H. Wang, D. Xue, W. Wang, J. Cheng, *Inorg. Chem. Front.* **2017**, *4*, 675.
[52] J. V. Vaghasiya, C. C. Mayorga-Martinez, J. Vyskočil, Z. Sofer, M. Pumera, *Adv. Funct. Mater.* **2020**, *30*, 2003673.
[53] M. Xia, J. Ning, D. Wang, X. Feng, B. Wang, H. Guo, J. Zhang, Y. Hao, *Chem. Eng. J.* **2021**, *405*, 126611.
[54] F. Yang, H. Guo, J. Zhang, N. Wu, M. Yang, Y. Chen, T. Zhang, L. Sun, W. Yang, *J. Energy Storage* **2022**, *54*, 105234.
[55] Q. Qin, L. Chen, T. Wei, X. Liu, *Small* **2019**, *15*, 1803639.
[56] T.-W. Lin, T. Sadhasivam, A.-Y. Wang, T.-Y. Chen, J.-Y. Lin, L. D. Shao, *ChemElectroChem* **2018**, *5*, 1024.
[57] S. Lee, J. Hwang, D. Kim, H. Ahn, *Chem. Eng. J.* **2021**, *419*, 129701.
[58] Z. Jiang, T. Xu, S. Dai, C. Yan, C. Ma, X. Wang, J. Xu, S. Zhang, Y. Wang, *Energy Technol.* **2019**, *7*, 1800476.
[59] S. Ivanova, E. Zhecheva, R. Kukeva, D. Nihtianova, L. Mihaylov, G. Atanasova, R. Stoyanova, *ACS Appl. Mater. Interfaces* **2016**, *8*, 17321.
[60] S. J. Marje, H. B. Tyagaraj, S.-K. Hwang, K. S. Ranjith, E. Alhajri, N. R. Chodankar, Y. S. Huh, Y.-K. Han, *J. Mater. Chem. A* **2024**, *12*, 7587.
[61] Y. Wang, X. Zhang, P. Xiong, F. Yin, Y. Xu, B. Wan, Q. Wang, G. Wang, P. Ji, H. Gou, *J. Mater. Chem. A* **2018**, *6*, 21605.